Electronic Supplementary Material (ESI) for Materials Chemistry Frontiers.

Electronic Supplementary Information

Carbon nanofiber-based catalysts derived from polyacrylonitrile for efficient oxygen reduction in alkaline and neutral Zn-air batteries

Min Lu, Xiumei Chen, Yu Xu, Ruigang Liu, Xiaoji Xie*

Key Laboratory of Flexible Electronics (KLOFE) & Institute of Advanced Materials (IAM)

Nanjing Tech University, Nanjing 211816, China

Email: iamxjxie@njtech.edu.cn

Experimental details

a. General characterization

Thermogravimetric analysis was carried out on a thermogravimetric analyzer (TGA2, Mettler Toledo) in the O_2 environment. Morphology was observed by a scanning electron microscope (JSM-7800F, JEOL), a transmission electron microscope (JEM-1400 plus, JEOL) and a high-resolution transmission electron microscope (JEM-2100F, JEOL). Fourier transform infrared (FTIR) spectra were recorded on a Bruker (Alpha) FTIR spectrometer. X-ray diffraction (XRD) analysis was carried out on an X-ray diffractometer (Smart Lab 9 kW, Rigaku). X-ray photoelectron spectroscopy (XPS) was performed on an ESCALAB 250Xi spectrometer (Thermo Scientific). The N_2-sorption isotherm, Brunauer-Emmett-Teller (BET) surface area, and pore volume of the materials were analyzed using a surface area and porosity analyzer (ASAP 2460, Micromeritics) at 77 K. Raman spectra were collected on a Raman spectrometer (iHR 550, Horiba). Electrochemical tests were carried out on an electrochemical workstation (Zennium, Zahner) equipped with a rotating ring-disk electrode (RRDE, E7R9 (Tip), Shaft (MSR), Pine Research Instrumentation).

b. Electrochemical measurements

To test the catalytic performance, the obtained catalysts were drop-casted onto the polished glassy carbon disk (diameter: 5.5 mm) of the RRDE to form a thin layer under steady rotation (700 rpm), reaching a certain loading amount (0.2 or 1.0 mg cm^{-2}).[S1] Meanwhile, the 20% Pt/C catalyst (Johnson Matthey) was used as the benchmark catalyst, and drop-casted by the same method for comparison. The catalyst-coated electrode was used as the working electrode for electrochemical characterizations in different electrolytes. Specifically, a KOH solution (0.1 M) was used as the alkaline electrolyte, and a phosphate

buffer (PB, 50 mM, a solution of 31.3 mM Na_2HPO_4 and 18.7 mM NaH_2PO_4, pH = 7) was used as the neutral electrolyte. Notably, a Pt mesh was used as the counter electrode and the Ag/AgCl/KCl (3 M) electrode was used as the reference electrode. Unless otherwise noted, the potential presented was converted into the reversible hydrogen electrode (RHE) scale using Equation S1.

$$E_{RHE} = E_{Ag/AgCl} + 0.21 + 0.059 \times \mathrm{pH} \quad \text{(S1)}$$

Before electrochemical tests, the electrolyte was purged with O_2 for 30 min to create an O_2-saturated environment. Linear sweep voltammetry (LSV) was carried out at a scan rate of 5 mV s^{-1} with rotating rates from 625 to 2500 rpm. On the basis of LSV result, 1/j was plotted against $\omega^{-1/2}$ according to Koutecky-Levich equation (Equation S2).

$$\frac{1}{j} = \frac{1}{j_L} + \frac{1}{j_K} = \frac{1}{Bw^{1/2}} + \frac{1}{j_K} \quad \text{(S2)}$$

where j is the current density of the glassy carbon disk (mA cm^{-2}), j_L and j_K are the limiting and kinetic current densities (mA cm^{-2}) respectively, ω is the rotation rate (rpm) of the disk, and B is defined by Equation S3.

$$B = 0.2nFC_0(D_0)^{2/3}\nu^{-1/6} \quad \text{(S3)}$$

where n is the electron transfer number, F is the Faraday constant, C_o is the bulk concentration of O_2, D_o is the diffusion coefficient of O_2, and ν is the kinematic viscosity of the electrolyte.

For the RRDE test, the disk current density (j_d) and ring current density (j_r) were recorded simultaneously. The scan rate was 5 mV s^{-1}, the rotating rate was 1600 rpm, and the ring potential was set as 1.50 V vs. RHE. On the basis of RRDE results, the H_2O_2

selectivity and electron transfer number (n) can be derived using the following equations (Equation S4 and S5).

$$H_2O_2 \text{ selectivity} = 2 \times \frac{j_r/N}{j_d+j_r/N} \quad \text{(S4)}$$

$$n = 4 \times \frac{j_d}{j_r/N+j_d} \quad \text{(S5)}$$

where j_d is the disk current density, j_r is the ring current density, and N is current collection efficiency of the Pt ring (38% as the measured value).

The stability of the catalysts was evaluated by accelerated durability test (ADT). Briefly, LSV was at first measured in O_2-saturated electrolytes, and measured again after 5000 cyclic scans (scan rate: 100 mV s^{-1}) for comparison. In the alkaline electrolyte (0.1 M KOH solution), the potential range for cyclic scan was set as 0.1 to -0.3 V (vs. Ag/AgCl/KCl (3 M)). In the neutral electrolyte (50 mM phosphate buffer), the potential range for cyclic scan was set as 0.2 to -0.2 V (vs. Ag/AgCl/KCl (3 M)). The methanol tolerance of the catalyst was evaluated by chronoamperometry during which methanol was added into the 0.1 M KOH electrolyte to reach the concentration of 1 M.

Electrochemical active surface area (ECSA) of the catalyst was measured on the catalyst-coated glassy carbon disk (0.2 mg cm^{-2}) by cyclic voltammetry (CV) in the non-Faradaic region based on the double-layer capacitance. Particularly, 0.1 M KOH was used as the electrolyte, the potential range was set as a 0.1 V window centered at the open circuit potential (e.g., -0.167 to -0.067 V vs. Ag/AgCl/KCl (3 M) for CNF-230), and the scan rates were set as 10, 15, 20, 25, 30 and 35 mV s^{-1}. The ECSA of the catalysts can be calculated from the electrochemical double-layer capacitance (C_{dl}) according to the Equation S6.[S2, S3]

$$\text{ECSA} = \frac{C_{dl}}{C_s} \quad \text{(S6)}$$

where C_{dl} is the slope of current density against scan rate, and C_s is the specific capacitance associated with smooth carbon catalysts (40 μF cm^{-2}).[S3]

c. Practical application in Zn-air batteries

The practical applications were carried out in both the alkaline and neutral Zn-air batteries.[S4] The Zn-air battery was assembled in a cubic configuration with the Zn plate anode (4.5 cm^2, thickness: 0.2 mm), and the carbon cloth cathode (1 cm^2) which was coated with polytetrafluoroethylene (13.5 mg cm^{-2}) on the air-facing side and catalyst (CNF-based catalysts: 1.0 mg cm^{-2} or Pt/C: 0.2 mg cm^{-2}) on the electrolyte-facing side. Between the anode and cathode, the distance was 1.4 cm, and the total volume of electrolyte was 4 mL. For the alkaline Zn-air battery, a solution containing KOH (6 M) and $Zn(CH_3COO)_2$ (0.2 M) was used as the electrolyte. For the neutral Zn-air battery, a solution containing NH_4Cl (4.0 M) and KCl (2.0 M) was used as the electrolyte, and the pH of the electrolyte was adjusted to 7 by $NH_3 \cdot H_2O$. The polarization curve was measured by LSV, and the scan rate was 5 mV s^{-1}.

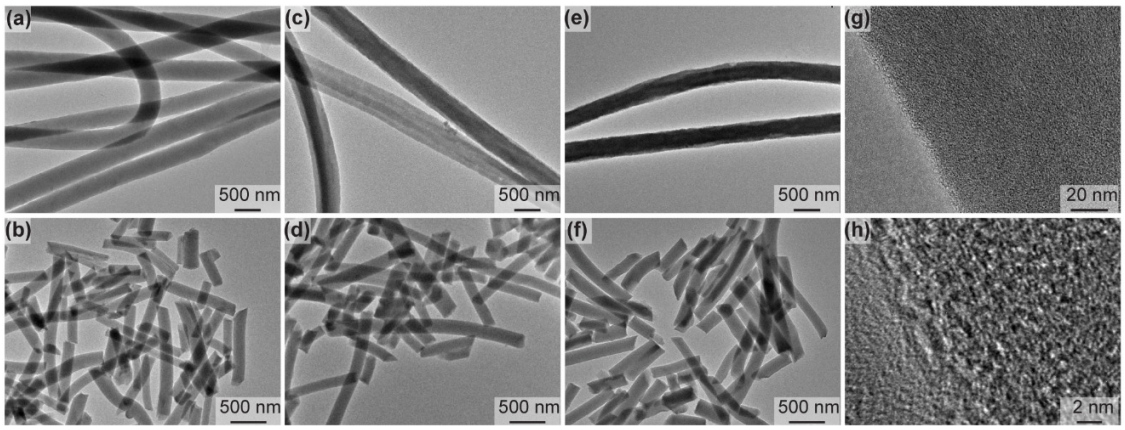

Figure S1. (a-f) TEM images of PAN-based materials and CNF-based catalysts. (a) PAN-230, (b) CNF-230, (c) PAN-230-H_2O, (d) CNF-230-H_2O, (e) PAN-230-H_2O_2, (f) CNF-230-H_2O_2. (g, h) High-resolution TEM images of CNF-230-H_2O_2.

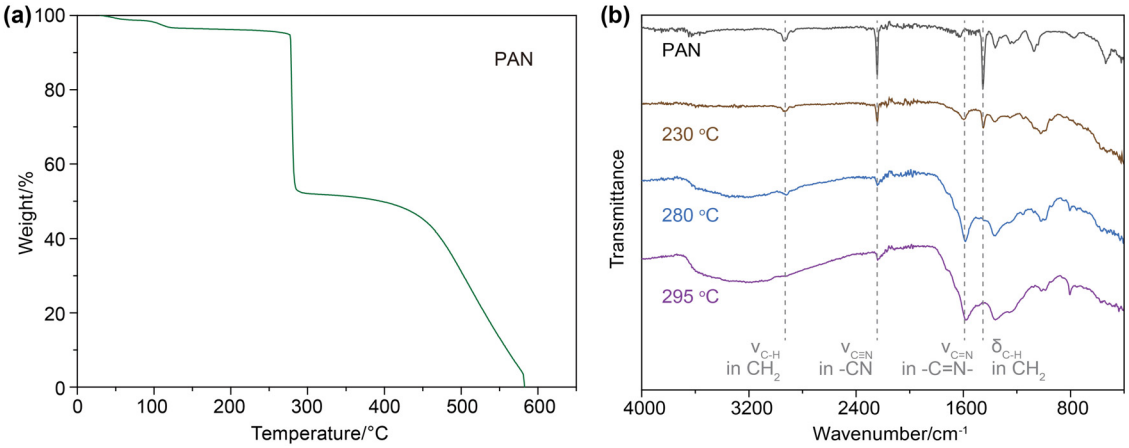

Figure S2. (a) TG curve of PAN mat in O_2 environment. (b) Fourier transform infrared spectra of PAN and PAN preoxidized at 230, 280, and 295 ºC in air.

The PAN was preoxidized at different temperatures in air for 1 h to study the structure evolution, and the resulting materials were characterized by infrared spectroscopy. As shown in Figure S2b, three characteristic peaks, attributed to the C-H stretch in CH_2 (~2931 cm^{-1}), C≡N stretch in CN (~2241 cm^{-1}) and C-H bending in CH_2 (~1452 cm^{-1}), decrease after proxidization.[S5,S6] Meanwhile, another peak appears at ~1579 cm^{-1}, which can be attributed to the C=N stretch in the –C=N– structure.[S6] The infrared spectra reveal the cyclization of the PAN structure to a six-membered ring-containing structure to different extents after the preoxidation at varied temperatures. To keep the cyclization at a relatively low level and to introduce more oxygen-containing groups in the next oxidation step, we chose 230 ºC as the preoxidation temperature.

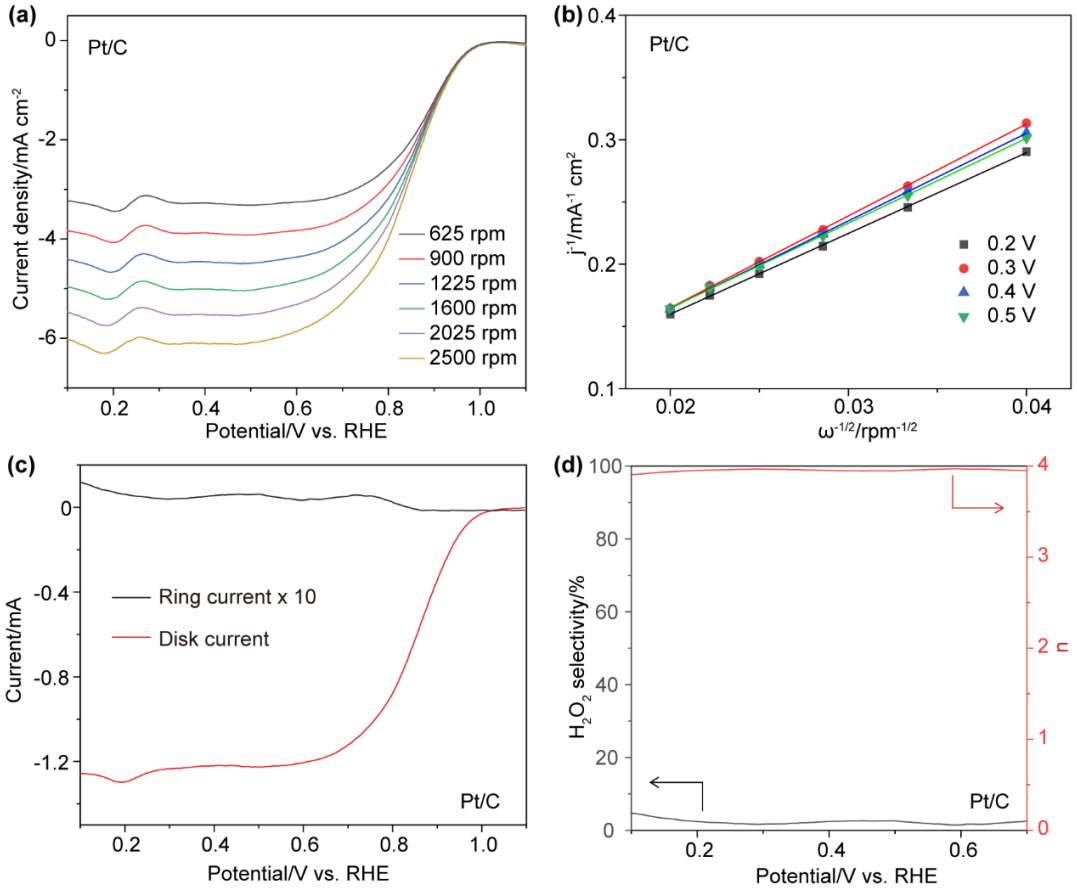

Figure S3. (a) Linear sweep voltammograms of the Pt/C catalyst at rotating rates of 625 to 2500 rpm in the O_2-saturated 0.1 M KOH. (b) The K-L plots corresponding to the linear sweep voltammograms in (a). (c) Ring and disk currents on a rotating ring-disk electrode using the Pt/C catalyst in the O_2-saturated 0.1 M KOH at a rotating rate of 1600 rpm. (d) H_2O_2 selectivity and electron transfer number based on ring and disk currents using the Pt/C catalyst.

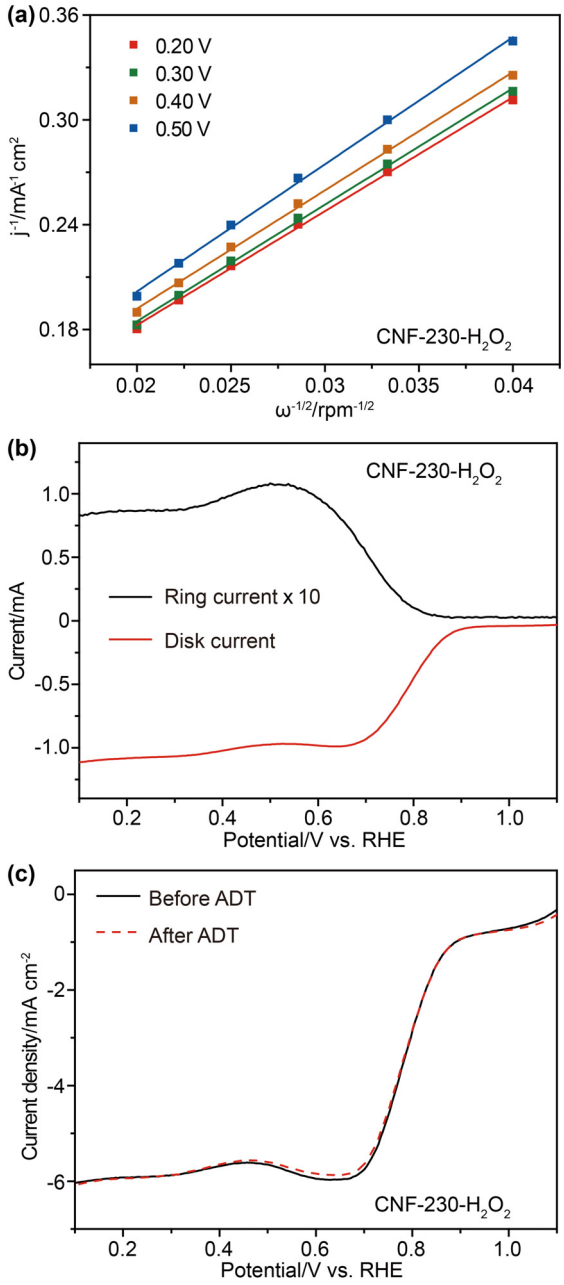

Figure S4. (a) The K-L plots corresponding to the linear sweep voltammograms in Figure 2b. (b) Ring and disk currents on a rotating ring-disk electrode using the CNF-230-H_2O_2 catalyst in the O_2-saturated 0.1 M KOH at a rotating rate of 1600 rpm. (c) Linear sweep voltammograms of the CNF-230- H_2O_2 catalyst before and after 5000 cyclic scans of the accelerated durability test (ADT) at a rotating rate of 1600 rpm.

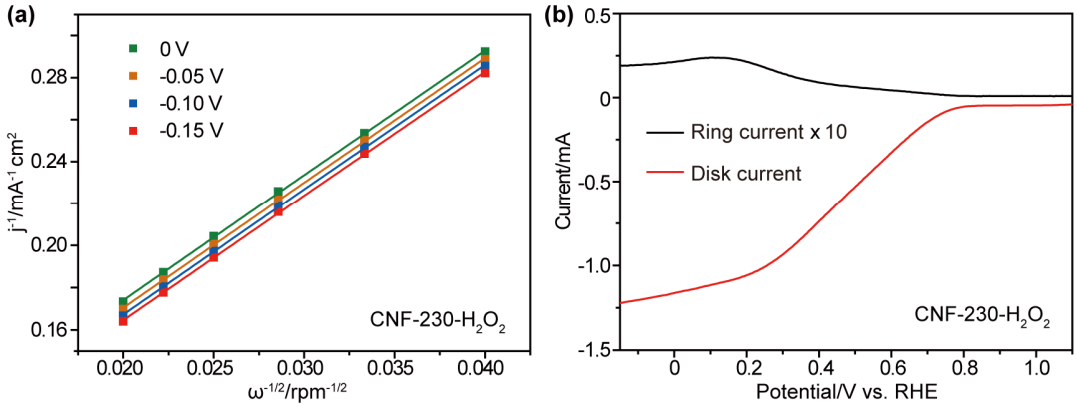

Figure S5. (a) The K-L plots corresponding to the linear sweep voltammograms in Figure 3c. (b) Ring and disk currents on a rotating ring-disk electrode using the CNF-230-H_2O_2 catalyst in the O_2-saturated 50 mM PB at a rotating rate of 1600 rpm.

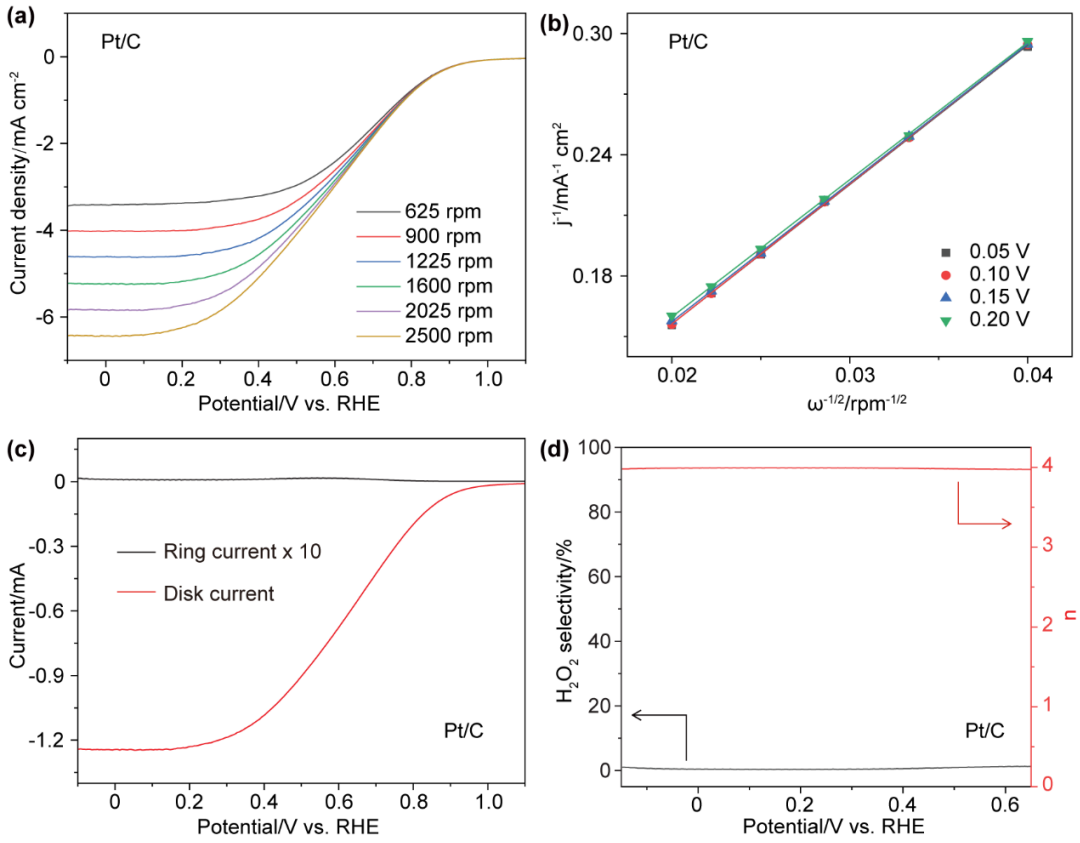

Figure S6. (a) Linear sweep voltammograms of the Pt/C catalyst at rotating rates of 625 to 2500 rpm in the O_2-saturated 50 mM PB. (b) The K-L plots corresponding to the linear sweep voltammograms in (a). (c) Ring and disk currents on a rotating ring-disk electrode using the Pt/C catalyst in the O_2-saturated 50 mM PB at a rotating rate of 1600 rpm. (d) H_2O_2 selectivity and electron transfer number based on ring and disk currents using the Pt/C catalyst.

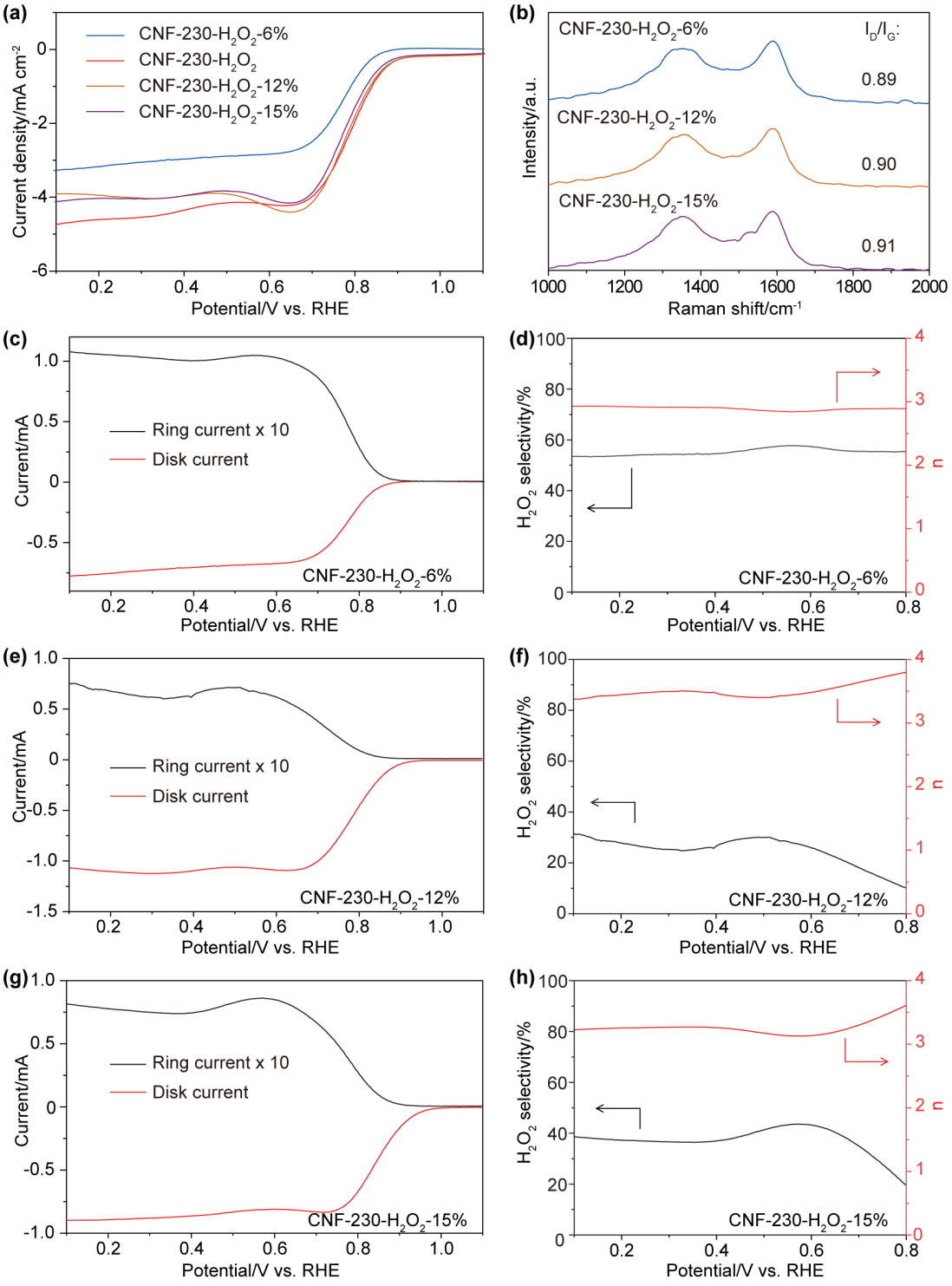

Figure S7. (a) Linear sweep voltammograms of CNF-based catalysts in the O_2-saturated 0.1 M KOH. The catalysts were obtained after the treatment in H_2O_2 aqueous solutions

with different H_2O_2 concentrations (6, 8.6, 12, and 15%) in the oxidation step during the preparation. (b) Raman spectra of the CNF-230-H_2O_2-6%, CNF-230-H_2O_2-12%, and CNF-230-H_2O_2-15% catalysts. (c, e, g) Ring and disk currents on a rotating ring-disk electrode using (c) CNF-230-H_2O_2-6%, (e) CNF-230-H_2O_2-12%, and (g) CNF-230-H_2O_2-15% catalysts in the O_2-saturated 0.1 M KOH at a rotating rate of 1600 rpm. (d, f, h) H_2O_2 selectivity and electron transfer number based on ring and disk currents using (d) CNF-230-H_2O_2-6%, (f) CNF-230-H_2O_2-12% and (h) CNF-230-H_2O_2-15% catalysts. Note: the CNF-230-H_2O_2 catalyst was treated in an 8.6% H_2O_2 solution in the oxidation step during the preparation.

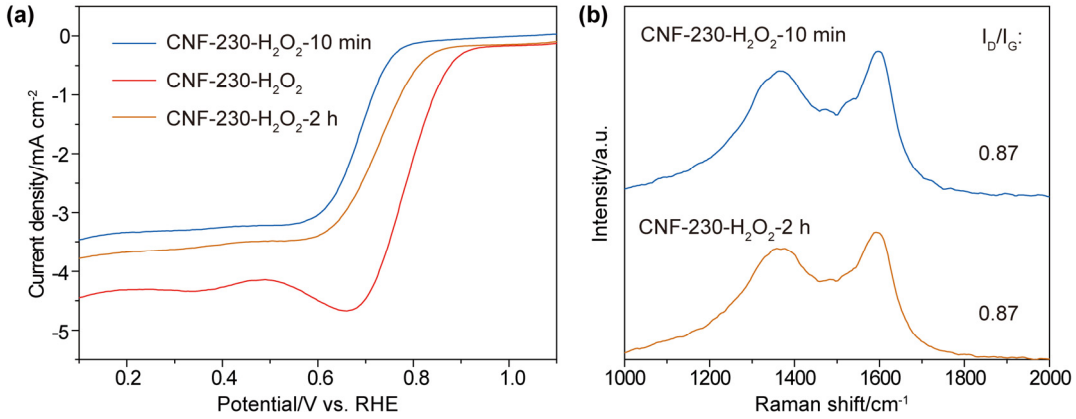

Figure S8. (a) Linear sweep voltammograms of CNF-based catalysts in the O_2-saturated 0.1 M KOH. The catalysts were obtained after the treatment in the 8.6% H_2O_2 aqueous solution for different durations (10 min, 1 h and 2 h) in the oxidation step during the preparation. (b) Raman spectra of the CNF-230-H_2O_2-10 min and CNF-230-H_2O_2-2 h catalysts. Note: the CNF-230-H_2O_2 catalyst was obtained after treated in the H_2O_2 solution for 1 h in the oxidation step during the preparation.

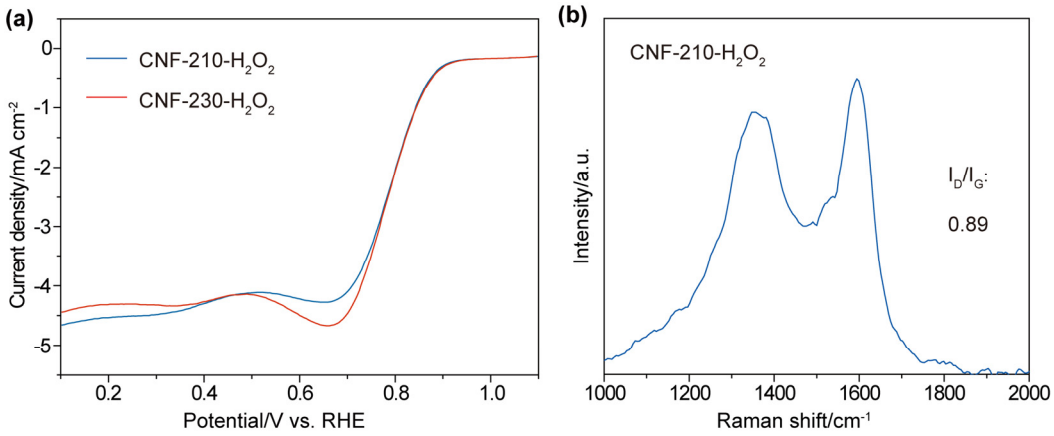

Figure S9. (a) Linear sweep voltammograms of CNF-based catalysts preoxidized at different temperatures (210 and 230 ℃) in the O_2-saturated 0.1 M KOH. (b) Raman spectrum of the CNF-210-H_2O_2 catalyst.

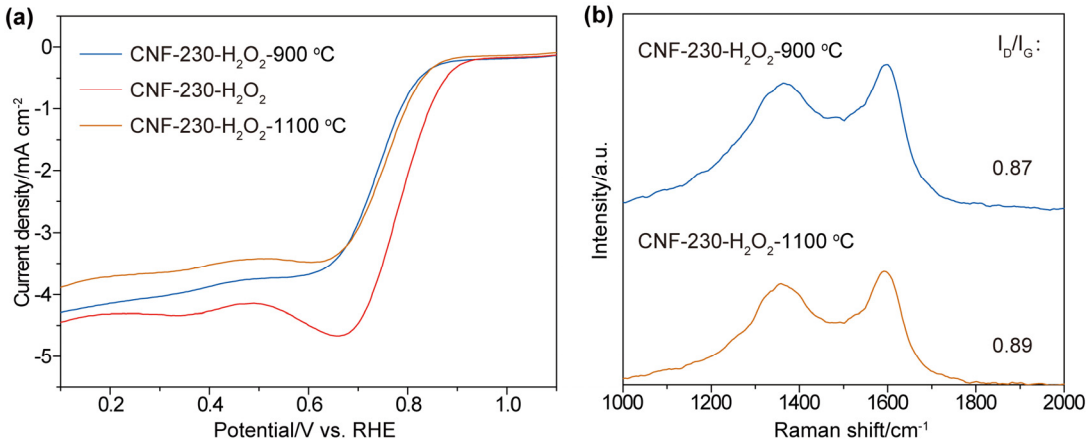

Figure S10. (a) Linear sweep voltammograms of CNF-based catalysts carbonized at different temperatures in the O_2-saturated 0.1 M KOH. (b) Raman spectra of the CNF-230-H_2O_2-900 °C and CNF-230-H_2O_2-1000 °C catalysts. Note: the CNF-230-H_2O_2 catalyst was carbonized at 1000 °C.

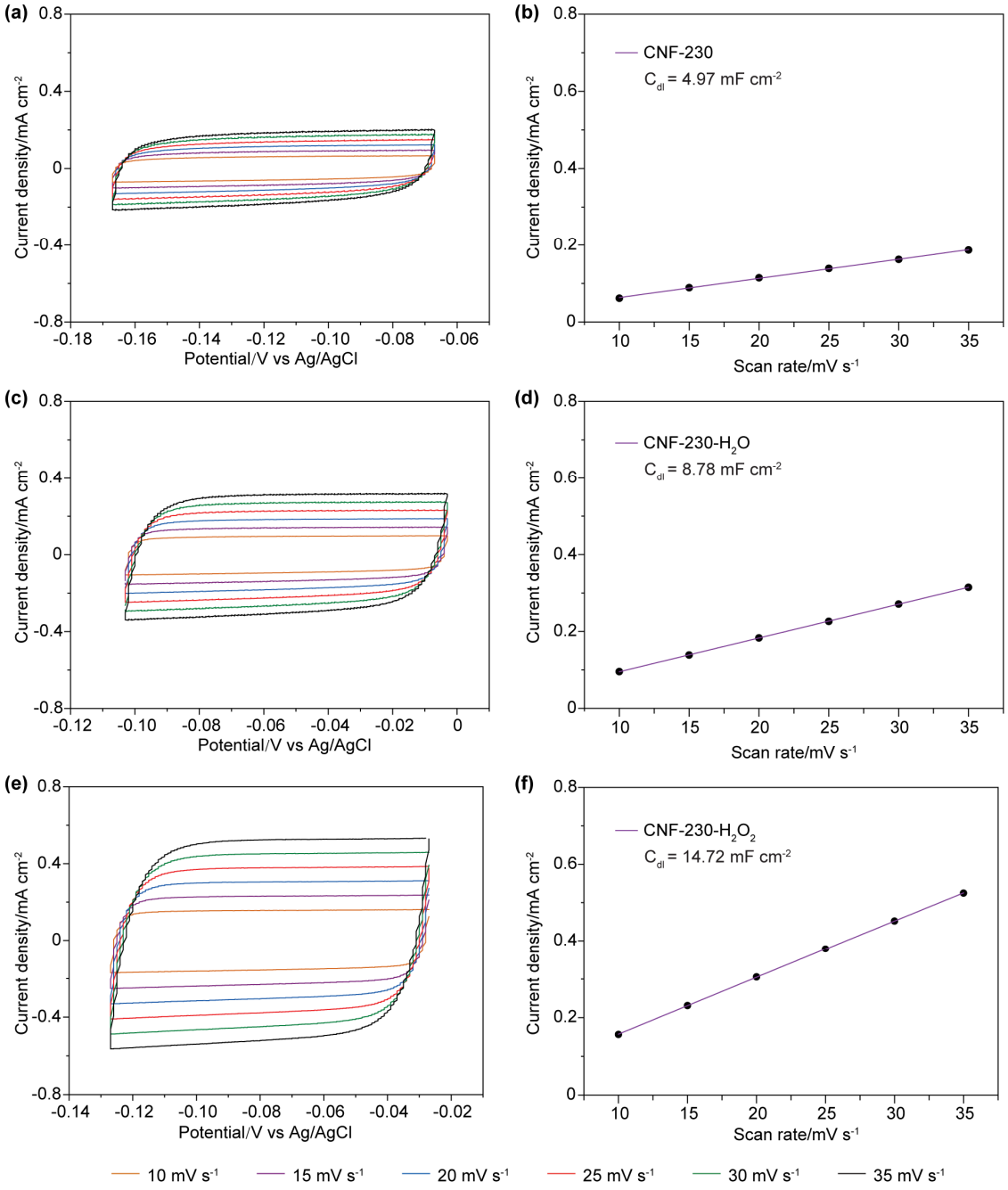

Figure S11. (a, c, e) CV curves in the non-Faradaic region of (a) CNF-230, (c) CNF-230-H_2O, and (e) CNF-230-H_2O_2 catalysts measured at different scan rates. (b, d, f) Corresponding current density-scan rate relationships of (b) CNF-230, (d) CNF-230-H_2O, and (f) CNF-230-H_2O_2 catalysts.

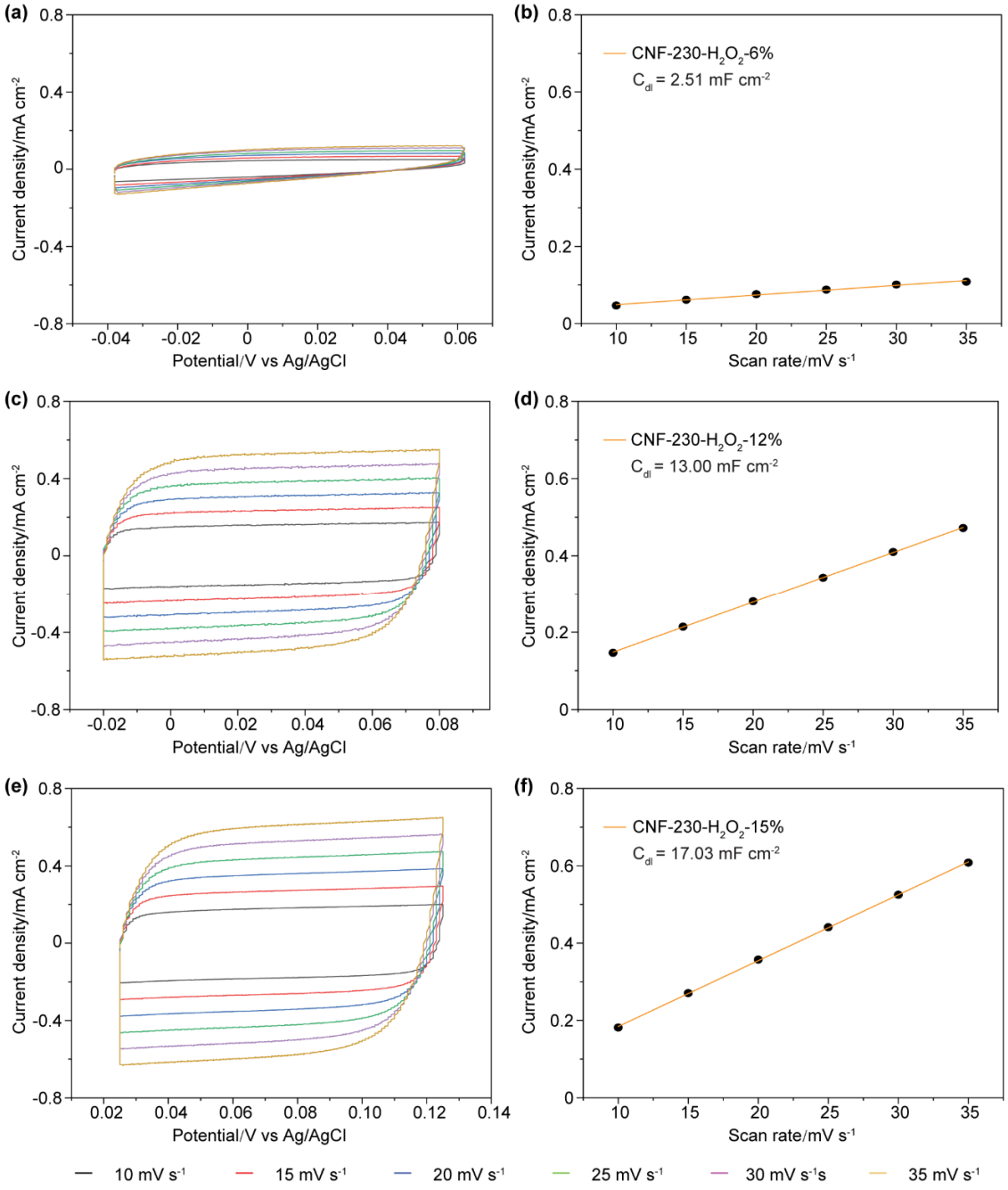

Figure S12. (a, c, e) CV curves in the non-Faradaic region of (a) CNF-230-H_2O_2-6%, (c) CNF-230-H_2O_2-12%, and (e) CNF-230-H_2O_2-15% catalysts measured at different scan rates. (b, d, f) Corresponding current density-scan rate relationships of (b) CNF-230-H_2O_2-6%, (d) CNF-230-H_2O_2-12%, and (f) CNF-230-H_2O_2-15% catalysts.

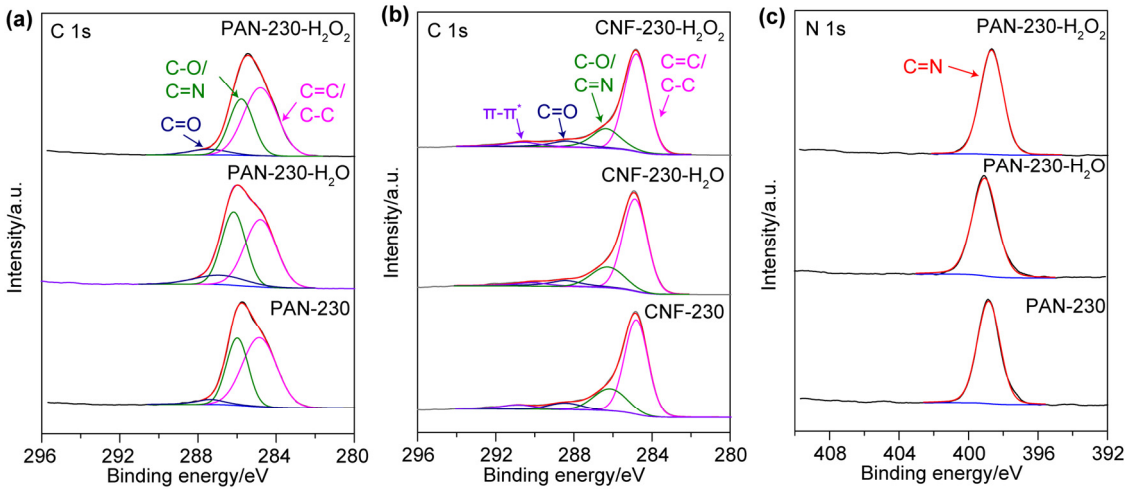

Figure S13. (a) High-resolution XPS spectra of the C 1s peak in PAN-based materials. (b) High-resolution XPS spectra of the C 1s peak in CNF-based catalysts. (c) High-resolution XPS spectra of the N 1s peak in PAN-based materials. Note: the peak heights in the figure were relative to the atomic ratios of C or N element in the corresponding material.

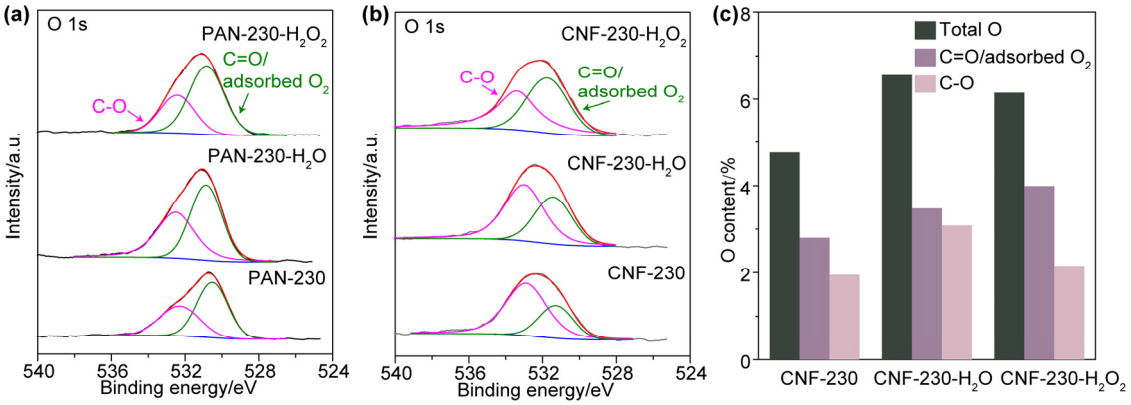

Figure S14. (a) High-resolution XPS spectra of the O 1s peak in PAN-based materials. (b) High-resolution XPS spectra of the O 1s peak in CNF-based catalysts. (c) O content in the PAN-based materials based on the deconvoluted O 1s spectra in (a). Note: the peak heights in the figure were relative to the atomic ratios of O in the corresponding material.

Table S1. The key experimental conditions used to convert PAN into PAN-based materials and CNF-based catalysts.

Samples	Temperature for peroxidation	Oxidation process at boiling temperature	Temperature for carbonization
PAN-230	230 ℃	-	-
PAN-230-H_2O_2	230 ℃	in 8.6% H_2O_2 for 1 h	-
PAN-230-H_2O	230 ℃	in H_2O for 1 h	-
CNF-230	230 ℃	-	1000 ℃
CNF-230-H_2O_2	230 ℃	in 8.6% H_2O_2 for 1 h	1000 ℃
CNF-230-H_2O	230 ℃	in H_2O for 1 h	1000 ℃
CNF-230-H_2O_2-6%	230 ℃	in 6% H_2O_2 for 1 h	1000 ℃
CNF-230-H_2O_2-12%	230 ℃	in 12% H_2O_2 for 1 h	1000 ℃
CNF-230-H_2O_2-15%	230 ℃	in 15% H_2O_2 for 1 h	1000 ℃
CNF-230-H_2O_2-10 min	230 ℃	in 8.6% H_2O_2 for 10 min	1000 ℃
CNF-230-H_2O_2-2 h	230 ℃	in 8.6% H_2O_2 for 2 h	1000 ℃
CNF-210-H_2O_2	210 ℃	in 8.6% H_2O_2 for 1 h	1000 ℃
CNF-230-H_2O_2-900 ℃	230 ℃	in 8.6% H_2O_2 for 1 h	900 ℃
CNF-230-H_2O_2-1100 ℃	230 ℃	in 8.6% H_2O_2 for 1 h	1100 ℃

Table S2. Electrochemical performance of catalysts for ORR in the O_2-saturated 0.1 M KOH.

Catalyst	E_{onset} (V)	$E_{1/2}$ (V)	j_{lim} (mA cm^{-2})
CNF-230 (0.2 mg cm^{-2})	0.727	0.696	2.95
CNF-230-H_2O (0.2 mg cm^{-2})	0.782	0.735	3.46
CNF-230-H_2O_2 (0.2 mg cm^{-2})	0.841	0.793	4.05
CNF-230-H_2O_2 (1 mg cm^{-2})	0.919	0.805	4.96
Pt/C (0.2 mg cm^{-2})	0.898	0.839	5.25

Table S3. Electrochemical performance of catalysts for ORR in the O_2-saturated 50 mM PB.

Catalyst	E_{onset} (V)	$E_{1/2}$ (V)	j_{lim} (mA cm^{-2})
CNF-230-H_2O_2 (0.2 mg cm^{-2})	0.650	0.484	4.45
CNF-230-H_2O_2 (1 mg cm^{-2})	0.737	0.450	5.89
Pt/C (0.2 mg cm^{-2})	0.802	0.594	5.62

Table S4. Comparison of ORR activity of the CNF-230-H_2O_2 catalyst with other PAN-based ORR catalysts reported previously in the O_2-saturated 0.1 M KOH (E_{onset} and $E_{1/2}$) and in fuel cell applications (P_{max}).

Catalyst	Precursor with optional additives	E_{onset} /V vs. RHE	$E_{1/2}$ /V vs. RHE	P_{max} /mW cm^{-2}	Ref.
PANRGO-700	PAN + graphene oxide	~0.89 *(~20 mV higher than Pt/C)*	0.864 *(~20 mV higher than Pt/C)*	116 *(10% lower than Pt/C)*	[S7]
Fe/IL-PAN-A1000	PAN + $Fe(OAc)_2$+ ionic liquid	0.95 *(30 mV lower than Pt/C)*	0.74 *(110 mV lower than Pt/C)*	289 *(18% lower than Pt/C)*	[S8]
Co-PAN-A1000	PAN + $Co(OAc)_2$	0.91 *(70 mV lower than Pt/C)*	0.74 *(110 mV lower than Pt/C)*	267 *(24% lower than Pt/C)*	[S8]
IL-Fe-PAN-900-0.75	PAN + ionic liquid	1.00 *(20 mV higher than Pt/C)*	0.85 *(30 mV higher than Pt/C)*	61	[S9]
FeZ-CNS-900	PAN + $ZnCl_2$ + $FeCl_3$	0.963 *(33 mV higher than Pt/C)*	0.881 *(39 mV higher than Pt/C)*	168 *(10% higher than Pt/C)*	[S10]
PAC/ZnO-900	PAN + ZnO	~0.902 *(22 mV higher than Pt/C)*	0.852 *(26 mV higher than Pt/C)*	NA	[S11]
NCNFs	PAN	~0.787 *(45 mV lower than Pt/C)*	~0.737 *(~70 mV lower than Pt/C)*	NA	[S12]
CNF-230-H_2O_2	PAN + H_2O_2	0.841 *(57 mV lower than Pt/C)*	0.793 *(46 mV lower than Pt/C)*	101 *(24% higher than Pt/C)*	This work

Table S5. Estimated cost of producing the CNF-230-H_2O_2 catalyst in industry.

	Precursor	Preoxidation	Oxidation	Carbonization	Other processes	Total
Cost ($/kg)	7.5	2.4	3	3.6	1.5	18

Note: Typically, the cost of producing PAN-based carbon nanofibers in industry is ~$15, which is comprised by the cost of precursor, preoxidation, carbonization, and other processes (such as sizing and winding).[S13,S14] In our method, we estimate that the additional oxidation process increases the total cost by ~20% according to the cost of preoxidation and carbonization.

References

[S1] S.S. Kocha, K. Shinozaki, J.W. Zack, D.J. Myers, N.N. Kariuki, T. Nowicki, V. Stamenkovic, Y. Kang, D. Li, D. Papageorgopoulos, Best practices and testing protocols for benchmarking orr activities of fuel cell electrocatalysts using rotating disk electrode, Electrocatalysis, 2017, 8, 366-374.

[S2] J. Kibsgaard, T.F. Jaramillo, Molybdenum phosphosulfide: an active, acid-stable, earth-abundant catalyst for the hydrogen evolution reaction, Angew. Chem., Int. Ed., 2014, 53, 14433-14437.

[S3] H. Fei, J. Dong, M.J. Arellano-Jiménez, G. Ye, N. Dong Kim, E.L.G. Samuel, Z. Peng, Z. Zhu, F. Qin, J. Bao, M.J. Yacaman, P.M. Ajayan, D. Chen, J.M. Tour, Atomic cobalt on nitrogen-doped graphene for hydrogen generation, Nat. Commun., 2015, 6, 8668.

[S4] Y. Xu, H. Zhang, P. Zhang, M. Lu, X. Xie, L. Huang, In situ exsolved Co components on wood ear-derived porous carbon for catalyzing oxygen reduction over a wide pH range, J. Mater. Chem. A, 2021, 9, 10695-10703.

[S5] I. Karacan, G. Erdogan, The influence of thermal stabilization stage on the molecular structure of polyacrylonitrile fibers prior to the carbonization stage, Fiber Polym., 2012, 13, 295-302.

[S6] S. Lee, J. Kim, B.-C. Ku, J. Kim, H.-I. Joh, Structural evolution of polyacrylonitrile fibers in stabilization and carbonization. Adv. Chem. Eng. Sci., 2012, 2, 275-282.

[S7] H. Begum, M.S. Ahmed, S. Jung, Template-free synthesis of polyacrylonitrile-derived porous carbon nanoballs on graphene for efficient oxygen reduction in zinc–air batteries, J. Mater. Chem. A, 2021, 9, 9644-9654.

[S8] G. Massaglia, A. Sacco, M. Castellino, A. Chiodoni, F. Frascella, S. Bianco, C.F. Pirri, M. Quaglio, N-doping modification by plasma treatment in polyacrylonitrile derived carbon-based nanofibers for oxygen reduction reaction, Int. J. Hydrogen Energy, 2021, 46, 13845-13854.

[S9] C. Wang, Q. Li, J. Guo, Y. Ren, J. Zhang, F. Yan, Metal-containing ionic liquid/polyacrylonitrile-derived carbon nanofibers for oxygen reduction reaction and flexible Zn–air battery, Chem.-Asian J., 2019, 14, 2008-2017.

[S10] G. Li, L. Pei, Y. Wu, B. Zhu, Q. Hu, H. Yang, Q. Zhang, J. Liu, C. He, Facile synthesis of polyacrylonitrile-based N/S-codoped porous carbon as an efficient oxygen reduction electrocatalyst for zinc–air batteries, J. Mater. Chem. A, 2019, 7, 11223-11233.

[S11] C. You, R. Zheng, T. Shu, L. Liu, S. Liao, High porosity and surface area self-doped carbon derived from polyacrylonitrile as efficient electrocatalyst towards oxygen reduction, J. Power Sources, 2016, 324, 134-141.

[S12] D. Liu, X. Zhang, Z. Sun, T. You, Free-standing nitrogen-doped carbon nanofiber films as highly efficient electrocatalysts for oxygen reduction, Nanoscale, 2013, 5, 9528-9531.

[S13] A.S. Gill, D. Visotsky, L. Mears, J. D. Summers, Cost estimation model for polyacrylonitrile-based carbon fiber manufacturing process, J. Manuf. Sci. Eng., 2017, 139, 041011.

[S14] S. Nunna, P. Blanchard, D. Buckmaster, S. Davis, M. Naebe, Development of a cost model for the production of carbon fibres, Heliyon, 2019, 5, e02698.